LAWRENCE
LIVERMORE
NATIONAL
LABORATORY

Demonstration of Symmetry Control of Infrared Heated Deuterium Layers in Hohlraums

B. J. Kozioziemski, R. A. London, R. L. McEachern, D. N. Bittner

August 22, 2003

Demonstration of symmetry control of infrared heated deuterium layers in hohlraums

B. J. Kozioziemski, R. A. London, and R. L. McEachern

Lawrence Livermore National Laboratory, Livermore CA 94551

D. N. Bittner

Schafer Corporation 303 Lindbergh Ave., Livermore CA 94551

(Dated: August 22, 2003)

Infrared smoothed deuterium ice layers inside capsules have been successfully demonstrated for capsules inside cylindrical hohlraums. Improved characterization methods and infrared illumination enables low mode control in both the axial and azimuthal directions. Experimental results agree well with computer models. Results of these experiments will be used to derive accuracy requirements for an infrared heating system for ice layers in hohlraums on NIF.

PACS numbers:

INTRODUCTION

Uniform hydrogen ice layers inside spherical plastic capsules produced by infrared (IR) illumination have been demonstrated for capsules in an integrating sphere[1, 2]. The capsules were uniformly illuminated by multiply scattered IR radiation while subject to spherical isotherms imposed by the integrating sphere geometry. The high vapor pressure of hydrogen near its triple point temperature enables rapid redistribution when the bulk is heated, thus forming smooth, uniform layers. Such targets are suitable for use in direct-drive inertial confinement fusion (ICF) experiments, such as at the University of Rochester Laboratory for Laser Energetics. In contrast, the National Ignition Facility (NIF) at Lawrence Livermore National Laboratory and the Laser Megajoule (LMJ) in France will initially explore indirect-drive, which requires spherical capsules placed inside cylindrical hohlraums. Solid deuterium (DD) and deuterium-tritium (DT) fuel layers must be smooth to within 0.5-1.0 μm RMS for a successful implosion[3]. The need for spherically symmetric ice layers inside the cylindrical geometry of a hohlraum makes layering of indirect-drive targets more complex than that of direct-drive targets.

Uniform heating of the ice layer inside a cylindrical hohlraum with uniform wall temperature leads to axial thickness variations. The dominant effect is in the Legendre P_2 mode, though all even modes will be present. An optical design was developed to illuminate the capsule with non-uniform IR to correct the P_2 asymmetry. This illumination design was described previously[4]. Briefly, a ring of IR is projected through each laser entrance hole (LEH) and onto the hohlraum wall. The roughened hohlraum wall scatters the IR in a nearly Lambertian angular distribution. A combination of optical and thermal models predicted that the ice layer shape could be controlled by the positioning of the injected IR along the hohlraum wall. The initial results were for one-sided illumination through one LEH of the hohlraum. Results presented in this paper include two-sided illumination, a hohlraum with improved scattering, and an additional characterization method to measure axial perturbations of the ice layer. Symmetry control was demonstrated using a combination of power balance and pointing of the IR inside the hohlraum. Computer models with parameters relevant to this experiment are compared to the experimental results.

MODELING

Computational modeling aided in the choice of parameter values to explore experimentally and was used in the interpretation of the experiments. A favorable comparison of calculated results to experiment provides confidence in the modeling techniques and therefore in calculations used to design future IR irradiation systems for NIF. Details of the modeling are presented in an accompanying paper[5]. Here we provide a brief description of the modeling rationale and methods and present results for the current experiments.

The main goal is to calculate the angular dependence of the heating of the capsule and D_2 ice and the resulting equilibrium ice distribution. The primary assumption is that the ice will redistribute itself inside the capsule so that the inner ice surface becomes isothermal. If the IR heating distribution and the heat transport out of the capsule were isotropic, then the ice layer would be spherical. However, in the current hohlraum with isothermal walls, the cylindrical shape leads to an anisotropic heat flow and tends to impose an asymmetry on the ice layer. One of the goals of IR irradiation is to heat the equator of the capsule and ice a bit more than the poles so as to cancel this transport effect and promote a spherical isotherm at the inner ice surface. An alternate method to control the hohlraum induced asymmetry is to impose a temperature gradient along the wall with heaters and cooling rings[6].

Raytrace

The scattering and absorption of the IR illumination is modeled using TracePro[7], a non-sequential, fully 3D ray tracing package. The reflective optics used to transport the IR are included with the model, along with the hohlraum, the capsule, and the ice layer inside the capsule. The best current values for the refractive indices and absorption coefficients for the capsule and ice are used, as well as a scattering model for the hohlraum based on measurements of rough gold surfaces (see Appendix A). Although the layering experiments usually involve IR injection through both laser entrance holes, the reflection symmetry of the system allows the simulation to use illumination from one side only. During a simulation, each ray is propagated until it leaves the model (i.e. exits from a laser entrance hole) or its energy drops below an arbitrary threshold (1% in our models). The program maintains a database for each of the inner and outer surfaces of the ice and capsule in which the intersection of a ray with that surface is recorded. The coordinates, energy, and direction of the ray are stored. These data are passed to an external program that calculates the energy deposition as a function of position within the capsule and ice. For a NIF-scale capsule (150-μm-thick capsule, 100-μm-thick ice layer), the capsule and ice are each resolved into 5 radial layers, 20 polar angles (the pole of the capsule is coincident with the axis of the hohlraum), and, in the case of 3D thermal modeling, 24 azimuthal angles. Most current experiments use a 40-μm-thick capsule with a 150-μm-thick ice layer, in which case the capsule is divided into 4 radial zones and the ice into 6.

Thermal calculation

The calculated IR power deposited in the capsule and ice are used as input for the thermal calculation to ultimately determine the ice layer shape. The temperature distribution in the hohlraum and capsule is calculated for the IR heating and conduction to the cooled hohlraum walls. This is done with the COSMOS program[8], using a steady-state finite element heat conduction package. Isothermal boundary conditions are applied on the hohlraum wall. Calculations for cases in which the IR optics are aligned with the hohlraum axis assume 2-D cylindrical symmetry. For the case of laterally offset IR beams, a 3-D geometry is used. Each heat conduction calculation is performed by assuming a certain ice layer distribution. Generally this is either a uniform spherical distribution, or a distribution wherein the ice thickness is perturbed by either a 1st or 2nd order Legendre polynomial (a P_1 or P_2). The temperature distribution on the inner surface of the ice is examined upon completion of the thermal calculation. It will in general not be isothermal. We then change the shape of the ice surface and recalculate the temperature field. If the changes are large, more than about 10 % in the ice thickness, both
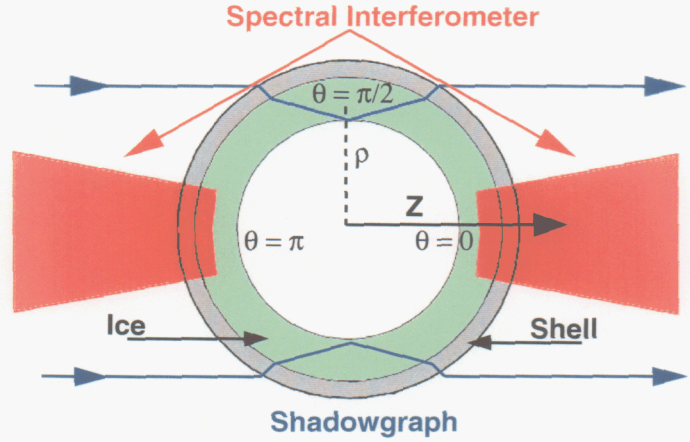

FIG. 1: Shadowgraph and spectral interferometry probe different regions of the capsule. Shadowgraph samples the ice thickness at $\theta = \pi/2$, while SI samples at $\theta = 0$ and $\theta = \pi$.

the ray tracing and the thermal transport are recalculated. Only the thermal transport is recalculated if the changes are small. We then reexamine the temperature on the inner ice surface. If it is not sufficiently isothermal, the surface is re-adjusted and another temperature calculation is performed. In practice, the temperature variations in the low order modes (P_1 and P_2) are found to be nearly linear functions of the thickness variations. Therefore, it suffices to perform 2-3 iterations of the ice thickness in order to find the (isothermal) equilibrium configuration.

CHARACTERIZATION METHODS

Optical access is available only through the hohlraum LEHs. Two methods where used to characterize the ice layer as illustrated in Fig. 1. The first, shadowgraphy, measures the ice uniformity in a plane through the equator of the capsule perpendicular to the hohlraum axis. The second, spectral interferometry (SI), measures the ice thickness at the poles of the capsule. Combining these two measurements provides limited axial characterization, effectively the lowest two modes. Both methods are described below.

Shadowgraphy

Shadowgraphy is frequently used for ICF target characterization[9–11]. A back-lighted target has a bright-band due to the total internal reflection at the ice–vapor interface. An analytical calculation maps the position of the bright band in the image to the actual ice layer thickness when the ice layer is spherical. This diagnostic was used to measure the ice symmetry at the mid-plane, $\theta = \pi/2$, as well as the average thickness.
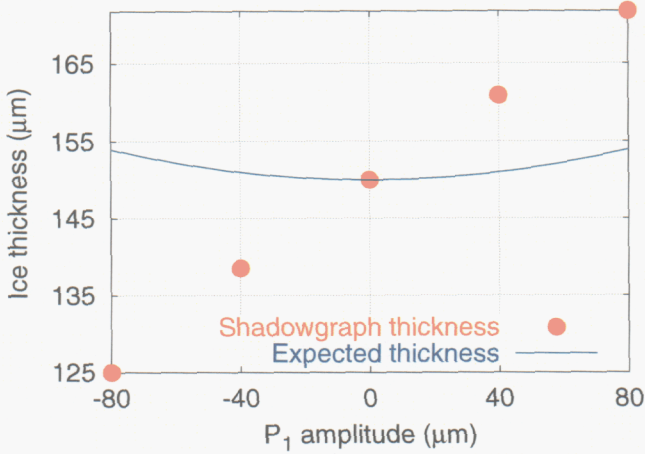
FIG. 3: Typical SI image. The low frequency fringes are the thinner capsule reflections and the higher frequency fringes are from the thicker ice layer. The vertical dimension is space along the capsule surface.

FIG. 2: A P_1 offset of the ice layer along the optical axis shifts the apparent position of the ice surface significantly compared to the actual thickness at the equator. The dots are from a TracePro raytrace of the shadowgraph optical system, and the line is the calculated ice thickness at the center of the shell for the given P_1.

To determine whether axial perturbations in the ice layer altered the bright band position for a given layer thickness, we modeled the effect of P_1 and P_2 perturbations on the apparent position of the ice layer with TracePro. We assumed a 150 μm thick ice layer inside of a 2 mm OD, 40 μm wall capsule, consistent with the experiment. We find that P_1 can significantly shift the apparent ice layer thickness. Figure 2 shows the thickness one would calculate from the bright band position (assuming a uniform layer) when a P_1 is imposed along the viewing axis. The optical effect is asymmetric with respect to zero offset and is fit by the second order equation

$$t_{\mathrm{apparent}} = 150.0 + 0.29A_1 - 2.7 \times 10^{-4}A_1^2 (\mu m), \quad (1)$$

where A_1 is the amplitude of the P_1 in μm. This offset is large compared to the expected layer thickness at the center of the shell, also shown in the figure. The optical effect of a P_2 was also modeled but found not to shift the bright band position. Therefore, the actual thickness at the equator was determined from the bright band in the shadowgraph image and corrections based on spectral interferometry thickness measurements at the poles.

Spectral interferometry

Spectral interferometry uses Fabry-Perot interference to determine optical thickness[12–14]. Light reflected from the shell–ice and ice–vapor interfaces constructively interferes when the optical thickness is an integer multiple of the wavelength. The intensity is a maximum when $m\lambda = 2nt$, where n is the refractive index of the ice, t is the ice thickness, and m is an integer. The thickness cannot be de-

termined from a single wavelength because the order of interference m is unknown. However, using white light to illuminate the capsule and dispersing the collected light with a spectrometer yields a series of bright and dark fringes. The difference $\Delta m = m_2 - m_1$ is obtained by counting the number of fringes between two known wavelengths λ_1 and λ_2. This difference is related to the thickness by

$$\Delta m = 2t \left(\frac{n(\lambda_2)}{\lambda_2} - \frac{n(\lambda_1)}{\lambda_1} \right). \quad (2)$$

Thus, t can be determined for known $n(\lambda)$.

The hydrogen refractive index is close to 1, so the amplitude of the reflected light is small. In transmission spectral interferometry, light reflected at the ice–vapor interface then the ice–capsule interface interferes with unreflected light. The signal is dominated by the unreflected light which saturates the CCD at low fringe contrast. In reflection spectral interferometry, the same reflected light signal is used, but interferes only with other reflected light, hence the fringe contrast is higher because the amplitude of the two signals is comparable. We record the reflected light rather than the transmitted because the signal-to-noise ratio can be made larger by longer signal integration. Similarly, the geometry allows only high f/# optics, hence only a relatively small patch on each pole of the capsule can be measured. There are two additional sets of interference fringes. The first is from interference between reflections at the outer capsule and capsule–ice interface, and the second from interference of reflections from the outer capsule and inner ice interfaces. These different signals can be distinguished by their frequency using Fourier analysis.

A typical SI image is shown in Fig. 3. The low frequency fringes correspond to the ≈ 40 μm plastic capsule while the higher frequency fringes are from the ≈ 150 μm thick ice layer. Each horizontal line of the image was Fourier transformed, windowed over the frequency region of the ice signal, and inverse transformed. The phase information from the inverse Fourier transform was unwrapped and fit to Eq. 2 for t over a range of wavelengths to avoid edge effects from the windowing.

The ice index of refraction as a function of wavelength was obtained using Souers' fit to data[15] with the solid density just below the triple-point temperature. Although the formula is a fit to liquid phase data, we follow Souers' recommendation that it is a reasonable choice for the solid

as well. The values used are likely within 2% of the correct values, producing a similar uncertainty in the thickness measurements. The uncertainty in n does not affect thickness differences between the two sides using SI. However, it does affect the axial mode determinations because it is combined with the shadowgraph measurement which scales differently with n.

Axial mode measurements

The ice thickness is determined at three axial points, $\theta = 0$, $\theta = \pi/2$, and $\theta = \pi$, using a combination of shadowgraphy and SI. Ice thickness variations perpendicular to the hohlraum axis, i.e. $t(\rho)$, are reduced close to zero by adjusting the IR pointing in ρ. Thus, the ice thickness in the axial direction is assumed to be a sum of Legendre modes,

$$t(\theta) = t_0 + \sum_i A_i P_i(\cos\theta), \qquad (3)$$

where t_0 is the average layer thickness and A_i is the amplitude of the ith Legendre polynomial. Because the thickness is measured at three points, the Legendre decomposition cannot be completely determined.

The thicknesses at the poles are

$$t(0) = t_0 + \sum_{i=\text{odd}} A_i + \sum_{j=\text{even}} A_j$$

and

$$t(\pi) = t_0 - \sum_{i=\text{odd}} A_i + \sum_{j=\text{even}} A_j. \qquad (4)$$

Further, $P_{\text{odd}}(\cos\pi/2) = 0$, so that we can only measure the sum of the odd modes and can obtain no information about the individual odd mode amplitudes. Thus, we take

$$\sum_{i=\text{odd}} A_i = \frac{t(0) - t(\pi)}{2}. \qquad (5)$$

The low modes will dominate, so that $\sum_{i=\text{odd}} A_i \approx A_1 + A_3$.

Similarly, individual even modes cannot be extracted from these three measurements. Since $P_{\text{even}} = 1$ at $\theta = 0$ and $\theta = \pi$ and $P_{\text{odd}} = 0$ at $\theta = \pi/2$, a sum of even modes can be written as

$$\sum_{j=\text{even}} A_j \left(1 - P_j(\cos\pi/2)\right) = \frac{t(0) + t(\pi)}{2} - t(\pi/2) \qquad (6)$$

where

$$P_{n=\text{even}}(\cos\pi/2) = (-1)^{n/2} \frac{1 \cdot 3 \cdot 5 \cdots (n-1)}{2 \cdot 4 \cdot 6 \cdots n}. \qquad (7)$$

Thus, without making specific assumptions about modes, we cannot determine the individual even modes. We expect that the lowest modes will dominate. For the purpose of comparing experiment to model, we directly compare thicknesses at the three points and assume mode 2 is the only even mode present.
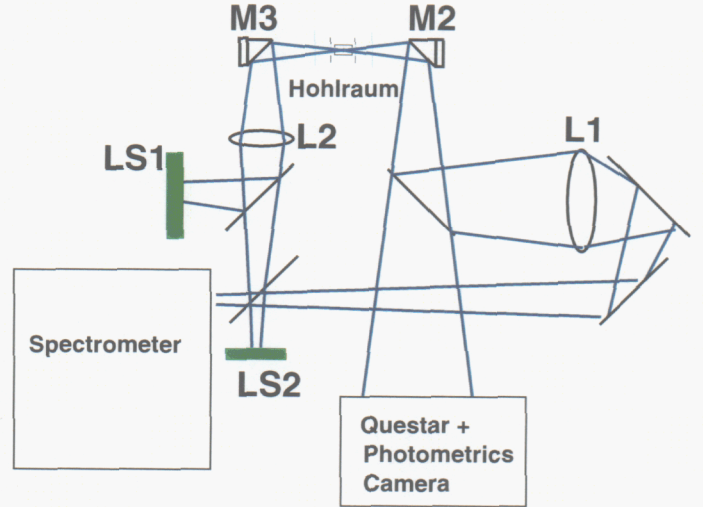

FIG. 4: Characterization optics layout. LS1 and LS2 are the light sources for shadowgraph and SI, respectively. LS2 is imaged onto a slit with the same width as the spectrometer entrance slit to limit heating of the capsule and subsequent movement of the ice layer. The Questar captures the shadowgraph image and the spectrometer the SI image.

EXPERIMENTAL SETUP

The current experiment is based on the apparatus described in ref. [4]. The notable differences are (1) the capsule is illuminated through both laser entrance holes, (2) an additional diagnostic was used to measure the thickness at the poles of the capsule and, (3) a gold hohlraum with 4 μm rms roughness and 11% absorption was soldered into a copper (OFHC) support to ensure efficient and uniform heat transport to the cryostat cold finger. Deuterium was used instead of deuterium-hydride. The IR illumination and shadowgraph optics are as shown in Fig. 5 of ref. [4], except the IR optics have been duplicated on the left side of the hohlraum and camera C2 was removed. The roughened surface provides diffuse scattering, but not as diffuse as a Lambertian scattering surface. Thermometers were placed at the center and at one end of the hohlraum as well as at the base of the support structure. The capsule is conductively cooled by ≈ 1 torr of helium exchange gas.

The characterization optics are shown schematically in Fig. 4. A Questar QM 100 long working distance microscope imaged the shell backlit by light source LS1 onto a 1024x1024 12-bit CCD camera with a typical resolution of 2.5 μm per pixel. The spectral interferometer setup enabled alternating measurements through each side of the hohlraum by placing a beam-block into one arm. The white light source LS2 is passed through a slit to limit the light on the shell to only that collected by the spectrometer. This prevents heating the capsule and possible movement of the ice. The reflected light is dispersed by a Chromex 250 IS imaging spectrometer onto an Andor DV420 CCD camera.
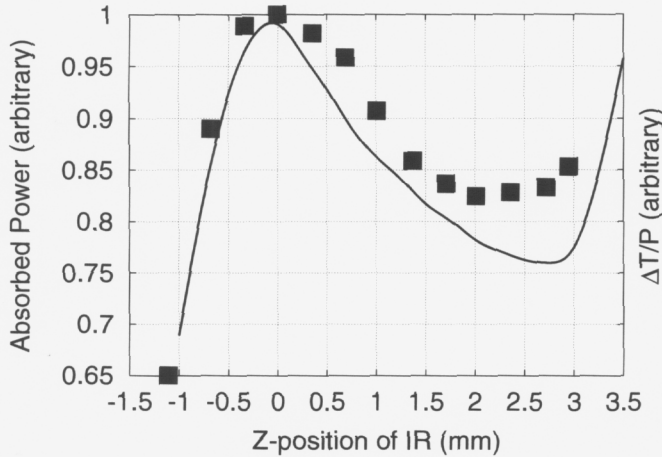
FIG. 5: Absorbed power calculated by the model (line) and the difference between the known and measured deuterium melting temperatures (squares) as the IR position along the hohlraum wall is varied. The measured temperature difference is normalized by the measured IR power entering the hohlraum.

The maximum entrance slit width was 75 μm.

The power balance was controlled using a pair of IR polarizers before the laser is coupled into the respective fibers. The power was measured for each polarizer pair and referenced to a common melting temperature of the ice.

IR pointing

The injected ring of IR must be positioned both along and perpendicular to the hohlraum axis. Initial alignment is performed by observing the visible light that co-propagates with the IR and aligning that light to the hohlraum LEH. Once the IR is aligned, hydrogen is admitted to the shell and frozen. The IR is then turned back on to redistribute the hydrogen. The IR ring is moved perpendicular to the axis until the layer is uniformly thick in the shadowgraph image. This is done for each side in turn.

The axial (Z-position) of the IR ring along the hohlraum wall was determined from the temperature drop, ΔT, between the capsule and the hohlraum wall and comparing to the raytrace models. The power absorbed by the capsule and ice is conducted away by the low pressure helium exchange gas to the hohlraum wall. Thus, ΔT is directly related to the total absorbed power. Melting of D_2 at the known temperature of T_m = 18.7 K is readily observed through the shadowgraphy system. ΔT is given by the difference of T_m and the measured hohlraum wall temperature T_H.

Figure 5 shows the raytrace model results for IR power absorbed by the capsule and ice as a function of Z-position along the hohlraum using only single-sided illumination.

The absorbed power starts at zero and increases as more of the IR ring passes through the LEH. At Z = 0, the IR is positioned at the hohlraum center and the maximum flux is absorbed by the capsule. As Z is further increased, the absorbed power decreases because less of the light scattered from wall directly illuminates the capsule. The rapid rise for Z > 3 mm is due to direct illumination of the capsule by the ring entering through the LEH. The experimentally measured ΔT, also shown in Fig. 5, follows the same shape as the absorbed power obtained from the raytrace model.

The Z = 0 position is defined as the peak in the curve. The Z position can be determined to within $\pm$ 200 μm in this way within a couple of hours. One difference between the model and the experiment is that the plateau region is higher for the experiment than for the model. This reflects imperfection in the optics, resulting in a slightly wider beam than the model used. Also, a persistent asymmetry in the IR illumination between the left and right side injection was observed. This difference could not be explained by different surface roughness of the left and right end-caps, nor by offsetting the capsule along the hohlraum axis. Its origin may lie in the quality of the optical surfaces and stray scattered light entering the hohlraum.

EXPERIMENTAL RESULTS

The IR injection enables control of the low mode axial and azimuthal modes of the ice layers. This control is accomplished with the combination of power balance and pointing of the IR inside of the hohlraum. The azimuthal offset is described first.

Azimuthal control

The ice offset from the hohlraum axis is controlled with the positioning of the IR. Ideally, the optical axis should be aligned with the hohlraum axis for azimuthal symmetry. The sensitivity of the ice layer to misalignment of the optical axis from the hohlraum axis is shown in Fig. 6. A P_1 is generated in the inner ice surface that is proportional to the IR pointing offset. The shadowgraph image gives the offset of the layer from the axis. Single sided illumination was used to simplify the interpretation of the results. The IR was pointed at Z = 2.0 mm to avoid clipping the IR ring at the hohlraum LEH. The least squares fit to the data is given by

$$A_1 = -0.35 - 0.018x, \qquad (8)$$

where x is the IR offset from the hohlraum axis and A_1 is the resulting ice layer offset, both in micrometers. The result of the model is shown for a 100 μm radial offset in the IR pointing. Our models indicate that for a given radial
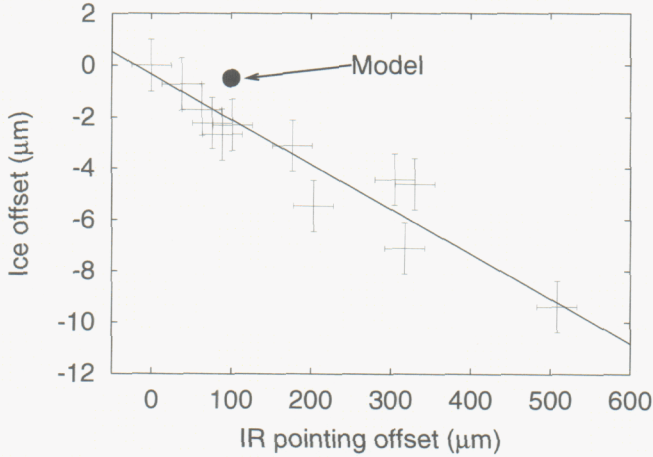
FIG. 6: Measured offset of ice layer from center of the capsule as a function of the IR pointing distance from the axis. The crosses represent the experimentally measured data and the solid circle is the model prediction. The data was shifted to have 0 μm ice offset at 0 μm IR pointing offset. The straight line is a least squares fit to the data.

offset of the IR, the layer offset depends on the IR position along Z, with a Z = 0 μm pointing giving an 11 μm ice layer offset in this case. The experimental uncertainty in Z-pointing of $\pm$ 200 μm thus corresponds to an uncertainty in the expected lateral offset of 1 μm. We therefore conclude that the observed shift is consistent with the model for the given parameters.

Axial Modes

As discussed above, we determine approximate values of the axial P_1 and P_2 amplitudes by combining the shadowgraphy and SI measurements. Control of the P_1 is accomplished by properly balancing the IR power entering through each LEH. Power in each beam line is adjusted until the thickness difference Δt between the left and right sides is minimized. The SI measured Δt is shown in Fig. 7 as a function of the relative difference in power ΔP between the two sides.

The fit function is $\Delta t = 9.1 + 0.74\Delta P$, where Δt is the thickness difference in micrometers and ΔP is the power imbalance calculated as $\Delta P = \frac{P_{\text{left}} - P_{\text{right}}}{P_{\text{left}} + P_{\text{right}}}$. Thus, keeping $\Delta t < 0.5$ μm requires the power balance to be within about 0.6%. The curve does not pass through the origin, reflecting the fact that the power is measured before the optical system which has slightly different efficiencies as well as variations through the cryostat windows. It may also represent a slight difference in the Z-position of the IR on each side, leading to different coupling efficiency to the capsule. For the extreme case of single sided injection, the model predicts $\Delta t = 64$ μm for $\Delta P = 100\%$, whereas the data shows a Δt of 65 μm and 83 μm depending on which side
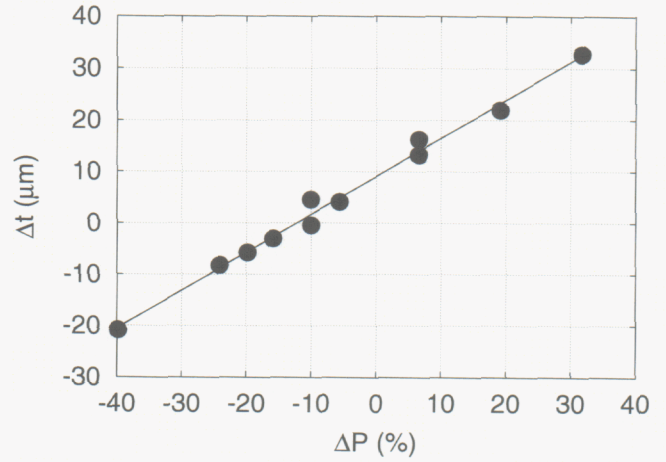

FIG. 7: Measured thickness difference Δt at the poles of the capsule as a function of the change in power balance ΔP. The straight line is a fit to the data described in the text.
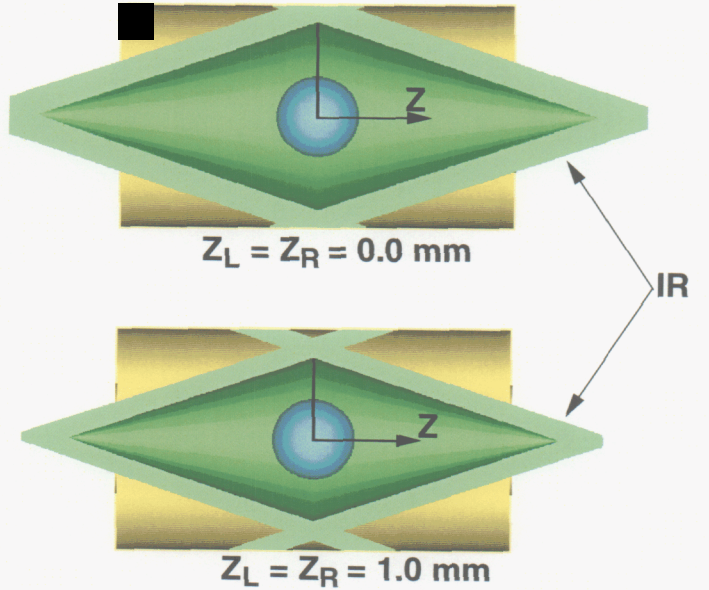

FIG. 8: IR pointing in the hohlraum for axial P_2 control. The first generates a layer that is equator hot while the second is closer to uniform heating.

is illuminated.

Varying the IR Z-position for both sides controls the P_2 amplitude of the ice layer. Figure 8 shows two particular IR pointings which demonstrate P_2 control. The first, at Z = 0 mm, heats the equator more than the poles and results in a layer thin at the equator. Thus, a modest P_2 is expected for the IR pointing of Z = 0 mm. The second, at Z = 1 mm, produces a more uniform temperature distribution along the ice surface, reducing the expected P_2 amplitude. Slightly different initial IR pointings than show in Fig. 8 were used in the experiment due to a small misalignment between the two sides. The P_2 values for a 1 mm change in IR point-
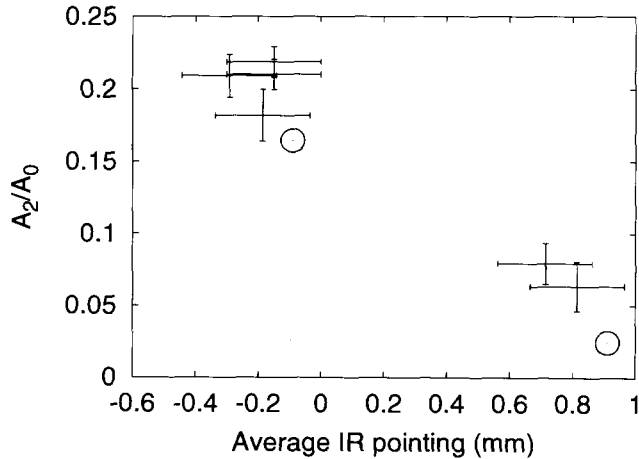
FIG. 9: Experimentally measured (crosses) and calculated (circles) ratio of P_2 to P_0 amplitudes for pairs of IR pointings.

ings are shown in Fig. 9. The average Z-position of the IR pointing for the two sides is used since the left and right sides were found to differ by about $\pm$ 0.2 mm from the average position. The decrease of A_2 as the Z-position of the IR is increased is clearly demonstrated in the experiment. The experimental data was measured for layers of 150 μm and 120 μm thick. Thus, the ratio of the A_2 to the average thickness A_0 shows that the effect is consistent with a thinner layer. In all cases, any P_1 was reduced to less than 1 μm by adjusting the power balance before recording the P_2 value. The model data, also shown in Fig. 9, shows a variation of P_2 amplitude with Z-position that is consistent with the experiment. The model included an offset in Z-position between the two sides consistent with the experiment.

CONCLUSIONS

Improved ice layer control using IR illumination has been demonstrated in this experiment. The addition of the spectral interferometry diagnostic enabled measurement of the ice layer movement along the hohlraum axis. This combined with the shadowgraph images provided P_1 and P_2 mode measurements of ice layers in the hohlraum. Locating the IR inside of the hohlraum was demonstrated using the change in temperature difference between the ice layer and the hohlraum as a function of the IR position. The P_1 and P_2 were shown to change with the IR pointing inside the hohlraum. The experimental results are consistent with model results using the currently best known parameters. Future work will explore layering of capsules without fill tubes and a more compact optical layout.

APPENDIX

To make TracePro simulations relevant to our experiments, realistic properties must be employed for the scattering surface inside the hohlraum. The specific quantity required for input to TracePro is the Bidirectional Reflectance Distribution Function (BRDF), defined as the scattered radiance per unit incident irradiance,

$$BRDF(\theta_i, \phi_i, \theta_s, \phi_s) = \frac{dL_s(\theta_s, \phi_s)}{dE_i(\theta_i, \phi_i)}. \qquad (9)$$

The units are inverse steradians. Note that for a perfect Lambertian surface, the BRDF is constant. The TracePro scattering model is based on one in which the BRDF is independent of the angle of incidence, being a function only of the difference between the scattered direction and the specular direction. This approach is known as the Harvey-Shack method[16]. Specifically, the independent variable is $|\vec{\beta} - \vec{\beta_0}|$, where $\vec{\beta}$ and $\vec{\beta_0}$ are the projections of the scattering and specular unit vectors onto the surface plane. TracePro parameterizes the scattering from a particular surface using the so-called ABg model, in which

$$BRDF = \frac{A}{B + |\vec{\beta} - \vec{\beta_0}|^g}. \qquad (10)$$

The A, B, and g parameters are determined by fitting to scattering data. For scattering in the plane of incidence, $|\vec{\beta} - \vec{\beta_0}|$ reduces to $|\sin(\theta) - \sin(\theta_0)|$, where θ and θ_0 are the scattered and specular angles with respect to the surface normal. It should be noted that the Harvey-Shack method is most appropriate for surfaces with roughness that is small compared to the wavelength of the light. For the much rougher surfaces under consideration here, there is no particular reason to expect it to be applicable. In fact, the measured BRDF can be quite dependent on the incident angle. TracePro accommodates this situation by allowing A, B, and g to depend on incident angle as well. This modification of the Harvey-Shack approach allows for much more flexibility in modeling realistic scattering behavior, although the ABg functional form does impose some constraints.

TABLE I: ABg coefficients used to model the roughened, 4μm RMS, gold hohlraum surface. The values were fit to the data shown in Fig. 10.

θ_i (deg.)	A	B	g	Absorbance
10	0.229	0.346	1.523	0.128
40	0.279	0.322	1.184	0.115
70	0.247	0.076	1.168	0.060

Because it is difficult to measure the scattering distribution from an actual hohlraum surface, a witness sample was prepared by electroplating gold onto a roughened OFHC
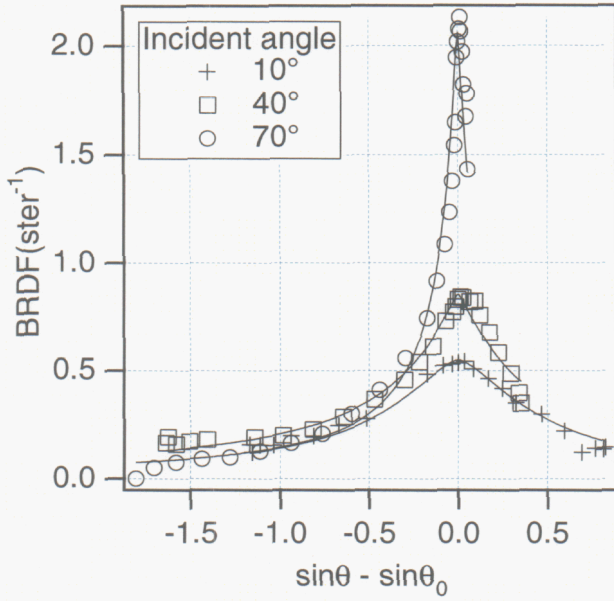
FIG. 10: BRDF curves measured for a roughened gold foil at three incident angles. Also shown are fits to these data using the ABg model.

copper disk, which was then etched away to leave a replica surface on a free-standing gold foil. The roughening process was identical to that used for the hohlraum mandrels. The in-plane scattering distribution for 3 μm light was measured for three incident angles: $10°$, $40°$, and $70°$. Figure 10 shows the results expressed as the BRDF versus $\sin(\theta) - \sin(\theta_0)$. Also shown are the ABg fits to each curve, where the actual ABg values are given in table I. The peak centered at $\sin(\theta) - \sin(\theta_0) = 0$ in each curve reflects the presence of an enhanced specular component. The curve fits for the measured angles are good, although data on out-of-plane scattering at angles far from specular deviate from the fits by up to a factor of two. To specify this surface in TracePro, values for B, g, and reflectance are entered for each of these incident angles (the requirement of energy conservation determines A). To calculate scattering from the surface at other incident angles, the program interpolates to find A, B, and g values for $10° < \theta_{\rm inc} < 70°$, and uses the $10°$ and $70°$ values for angles less than $10°$ and greater than $70°$, respectively.

[1] D. N. Bittner, G. W. Collins, E. Monsler, and S. Letts, Fusion Technology **35**, 244 (1999).
[2] D. N. Bittner, G. W. Collins, and J. D. Sater, Fusion Science and Technology **TBP** (2003).
[3] J. Lindl, Physics of Plasmas **2**, 3933 (1995).
[4] B. J. Kozioziemski, R. L. McEachern, R. A. London, and D. N. Bittner, Fusion Science and Technology **41**, 296 (2002).
[5] R. A. London, R. L. McEachern, B. J. Kozioziemski, and D. N. Bittner, TBP .
[6] J. J. Sanchez and W. H. Giedt, Fusion Tech. **36**, 346 (2000).
[7] Raytracing was performed using the TracePro$^{\rm TM}$ commercial optical modeling program. For further information contact Lambda Research Corp., Littleton, MA 01460.
[8] Thermal modeling was performed using the COSMOS commercial finite element method program. For further information contact Structural Research & Analysis Corp. Los Angeles, CA 90025.
[9] J. K. Hoffer, L. R. Foreman, J. J. Sanchez, E. R. Mapoles, and J. D. Sheliak, Fusion Tech. **30**, 529 (1996).
[10] J. A. Koch, T. P. Bernat, G. W. Collins, B. A. Hammel, B. J. Kozioziemski, A. J. MacKinnon, J. D. Sater, D. N. Bittner, and Y. Lee, Fusion Technology **38**, 123 (2000).
[11] J. A. Koch, T. P. Bernat, G. W. Collins, B. A. Hammel, J. D. Sater, and D. N. Bittner, Fusion Science and Technology **43**, 55 (2003).
[12] R. Le Toullec, P. Loubeyre, and J.-P. Pinceaux, Phys. Rev. B **40**, 2368 (1989).
[13] P. G. Johannsen, G. Reib, U. Bohle, J. Magiera, R. Muller, H. Spiekermann, and W. B. Holzapfel, Phys. Rev. B **55**, 6865 (1997).
[14] J. H. Eggert, L. Xu, R. Che, and L. Chen, J. Appl. Phys. **72**, 2453 (1992).
[15] P. C. Souers, *Hydrogen Properties for Fusion Energy* (University of California, Berkeley, 1986).
[16] J. E. Harvey, *Light-Scattering Properties of Optical Surfaces*, Ph.D. thesis, Univ. of Arizona (1976).